Mode-1 N_2 internal tides observed by satellite altimetry

Zhongxiang Zhao[1, 2]

[1]Applied Physics Laboratory, University of Washington, Seattle, Washington, USA
[2]School of Oceanography, University of Washington, Seattle, Washington, USA

Correspondence: Zhongxiang Zhao (zzhao@uw.edu)

Abstract. Satellite altimetry provides a unique technique for observing the sea surface height (SSH) signature of internal tides from space. Previous studies have constructed empirical internal tide models for the four largest tidal constituents M_2, S_2, K_1 and O_1 by satellite altimetry. Yet no empirical models have been constructed for minor tidal constituents. In this study, we observe mode-1 N_2 internal tides (the fifth largest constituent) using about 100 satellite-years of SSH data from 1993 to 2019. We employ a recently-developed mapping procedure that includes two rounds of plane wave analysis and a two-dimensional bandpass filter in between. The results show that mode-1 N_2 internal tides have mm-scale SSH amplitudes. Model errors are estimated from background internal tides that are mapped using the same altimetry data, but with a tidal period of 12.6074 hours (N_2 minus 3 minutes). The global mean error variance is about 25% that of N_2, suggesting that the mode-1 N_2 internal tides can overcome model errors. We find that the N_2 and M_2 internal tides have similar spatial patterns, and that the N_2 amplitudes are about 20% of the M_2 amplitudes. Both features are determined by the N_2 and M_2 barotropic tides. The mode-1 N_2 internal tides are observed to propagate hundreds to thousands of kilometers in the open ocean. The globally integrated N_2 and M_2 internal tide energies are 1.8 and 30.9 PJ, respectively. Their ratio of 5.8% is larger than the theoretical value of 4%, because the N_2 internal tides contain relatively large model errors. Our mode-1 N_2 internal tide model is evaluated using independent satellite altimetry data in 2020 and 2021. The results suggest that the model can make internal tide correction for SWOT in regions where the model variance is greater than twice the error variance. This work demonstrates that minor internal tidal constituents can be observed using multiyear multisatellite altimetry data and dedicated mapping techniques.

1 Introduction

The Moon's elliptical orbit around the Earth has an eccentricity of $\approx$0.055, with its perigean and apogean distances being about 3.63×10^5 and 4.06×10^5 km, respectively. The Moon completes one revolution every 27.5546 days (one anomalistic month). The tidal constituents L_2 and N_2 are induced by the Moon's elliptical orbit (Doodson, 1921). They are named the smaller and larger lunar elliptical semidiurnal constituents. The L_2 and N_2 periods are 12.1916 and 12.6583 hours, respectively (Doodson, 1921; Pawlowicz et al., 2002). M_2 (12.4206 hours) is based on the mean distance between the Earth and the Moon (3.84×10^5 km). While the L_2 and N_2 superposition gives the 27.5546-day perturbation with the Moon-Earth distance changes along the elliptic orbit. On global average, the amplitudes of M_2, N_2, and L_2 have a respective ratio of 1 : 0.2 : 0.05. N_2 is the fifth largest tidal constituent; therefore, its impact on the ocean environment is significant. For example, in waters around New Zealand, the N_2 barotropic tide has larger amplitudes than S_2 (Byun and Hart, 2020, Figure 4 therein). The superposition of N_2, M_2, L_2,

and S_2 can cause perigean spring tides (king tides) and apogean neap tides, which significantly affect harbors, coastal regions, and estuaries (Wood, 1978). Including N_2 internal tides can simulate the temporal variation of internal tide energetics with the Moon's elliptical motion. Theoretically, N_2 may modulate M_2 internal tides by $\pm20\%$ in amplitude, and by $\pm40\%$ in energy. On average, N_2 will enhance the M_2-induced ocean mixing by 4%.

Internal tides are widespread in the ocean and affect numerous ocean processes such as diapycnal mixing, tracer transport and acoustic transmission (Wunsch, 1975; Dushaw et al., 1995; Whalen et al., 2020). Internal tides may provide about half of the power for diapycnal mixing in the ocean interior (Munk and Wunsch, 1998; Egbert and Ray, 2000; MacKinnon et al., 2017; Kelly et al., 2021). The magnitude and geography of diapycnal mixing modulate the large-scale ocean circulation and global climate change; therefore, it is important to study their generation, propagation, and dissipation in the global ocean (Jayne and St. Laurent, 2001; Melet et al., 2016; Pollmann et al., 2019; Vic et al., 2019; de Lavergne et al., 2020; Arbic, 2022). Internal tides are annoying noise in the study of mesoscale and sub-mesoscale dynamics. In particular, it will be necessary to make internal tide correction to the Surface Water and Ocean Topography (SWOT) data, so that one can better study the sub-mesoscale dynamic processes (Fu and Ubelmann, 2014; Qiu et al., 2018; Wang et al., 2018; Morrow et al., 2019). Empirical internal tide models can be constructed using past satellite altimetry sea surface height (SSH) measurements. However, previous satellite observations focus mainly on the four largest tidal constituents M_2, S_2, K_1 and O_1 (Dushaw, 2015; Ray and Zaron, 2016; Zhao et al., 2016; Zaron, 2019; Ubelmann et al., 2022). Dushaw (2015) attempts to map N_2 internal tides using the TOPEX/Poseidon data from 1992 to 2008, but fails to obtain an empirical model, because the resulting N_2 internal tides are too noisy (see his Figures 38 and 52). That work is mainly limited by the short data set available then. In this study, we will construct a reliable empirical N_2 internal tide model using a larger data set and a recently-developed mapping method.

The challenge of observing N_2 internal tides by satellite altimetry lies in their small SSH displacements (Dushaw, 2015). Given that M_2 internal tides have SSH amplitudes of 1–2 cm, N_2 internal tides have only sub-centimeter SSH amplitudes. In this paper, the observation of N_2 internal tides is made possible by two improvements. First, a larger SSH data set becomes available, thanks to 27 years of multiple satellite observations from 1993 to 2019. The merged data set is about 100 satellite-years long; therefore, nontidal errors can be significantly suppressed. Second, a recently-developed mapping procedure is employed. This mapping technique extracts N_2 internal tides utilizing their known frequency and theoretical wavelengths. Nontidal errors can be significantly suppressed by both temporal and spatial filters. The resulting N_2 internal tides reveal their basic features in the global ocean, although they are still noisy (compared to the much larger M_2 internal tides). It is challenging (though possible) to extract L_2 internal tides, which are estimated to have 1-mm SSH signals at most (5% of M_2).

The rest of this paper is arranged as follows. Section 2 describes the data and methods used in this paper. Section 3 presents and discusses the new N_2 internal tides, mainly by comparing with the well-studied M_2 internal tides. Section 4 is a summary.
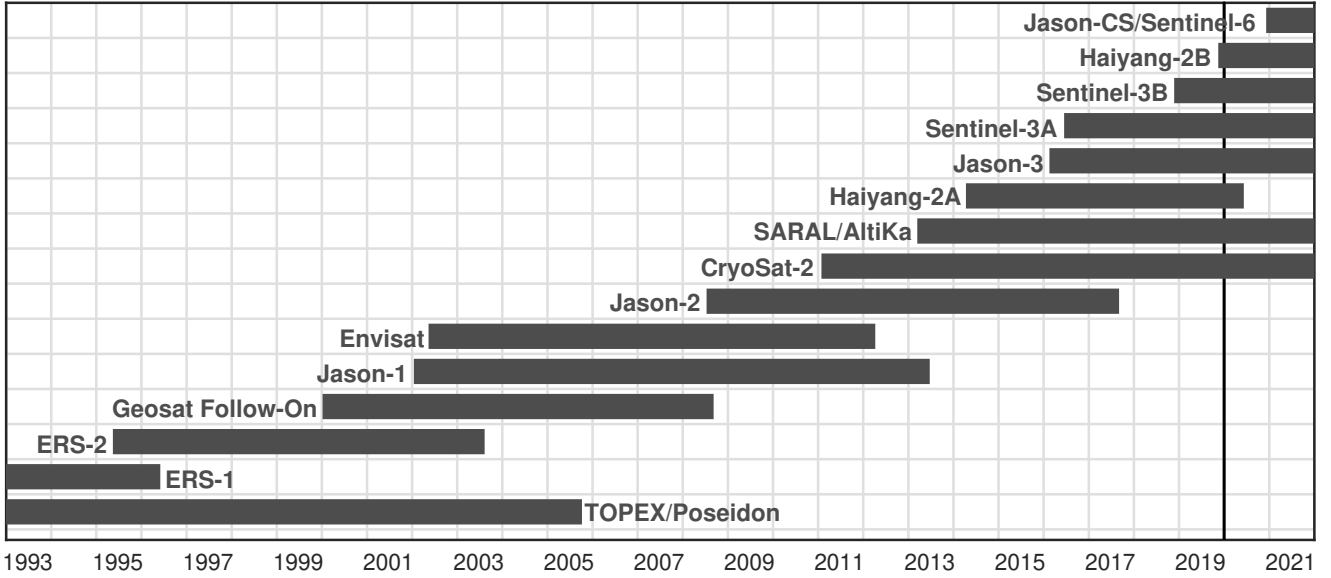
2 Data and methods

Figure 1. Satellite altimetry data used in this study. The merged multiyear multisatellite data from 1993 to 2019 are about 100 satellite-years long. The altimetry data in 2020 and 2021 are taken as independent data for model evaluation.

2.1 Data

The satellite altimetry SSH data used in this paper are collected by multiple altimetry missions from 1993 to 2019. In the order
60 of launch time, they are TOPEX/Poseidon, ERS-1, ERS-2, Geosat Follow-On, Jason-1, Envisat, Jason-2, CryoSat-2, SAR-AL/AltiKa, Haiyang-2A, Jason-3, Sentinel-3A, Sentinel-3B, Haiyang-2B and Jason-CS/Sentinel-6 (Figure 1). The combined data set is about 100 satellite-years long. We use the satellite along-track SSH data downloaded from the Copernicus Marine Service (https://doi.org/10.48670/moi-00146). The SSH measurements have been processed by standard corrections for atmospheric effects, surface wave bias, and geophysical effects (Pujol et al., 2016; Taburet et al., 2019). The ocean barotropic tide,
65 polar tide, solid Earth tide and loading tide are corrected using theoretical or empirical models (Pujol et al., 2016). Mesoscale correction (Ray and Byrne, 2010; Zhao, 2022a) is made using the gridded SSH fields downloaded from the Copernicus Marine Service (https://doi.org/10.48670/moi-00148). The satellite along-track SSH data in 2020 and 2021 are used to evaluate the new N_2 internal tide model as independent data (Section 2.6). Extracted from the 27-year-long data, our N_2 internal tide model contains only the 27-year-long coherent component. Their temporal variations (or incoherent components) are not addressed
70 in this paper.

The observation of internal tides by satellite altimetry may be affected by an issue called tidal aliasing, because the satellite repeat cycles are much longer than the semidiurnal and diurnal tides. Here we examine possible tidal aliasing issues with N_2 and M_2 internal tides. In one 160 km by 160 km fitting window (section 2.2), there are typically about 7.84×10^4 SSH data from multiyear multisatellite measurements. Using their observation times, we can calculate their phase lags with respect to
75 the N_2 tidal cycle (12.6583 hours). Figure 2a gives the histogram of their phase lags over one N_2 tidal cycle. For comparison,
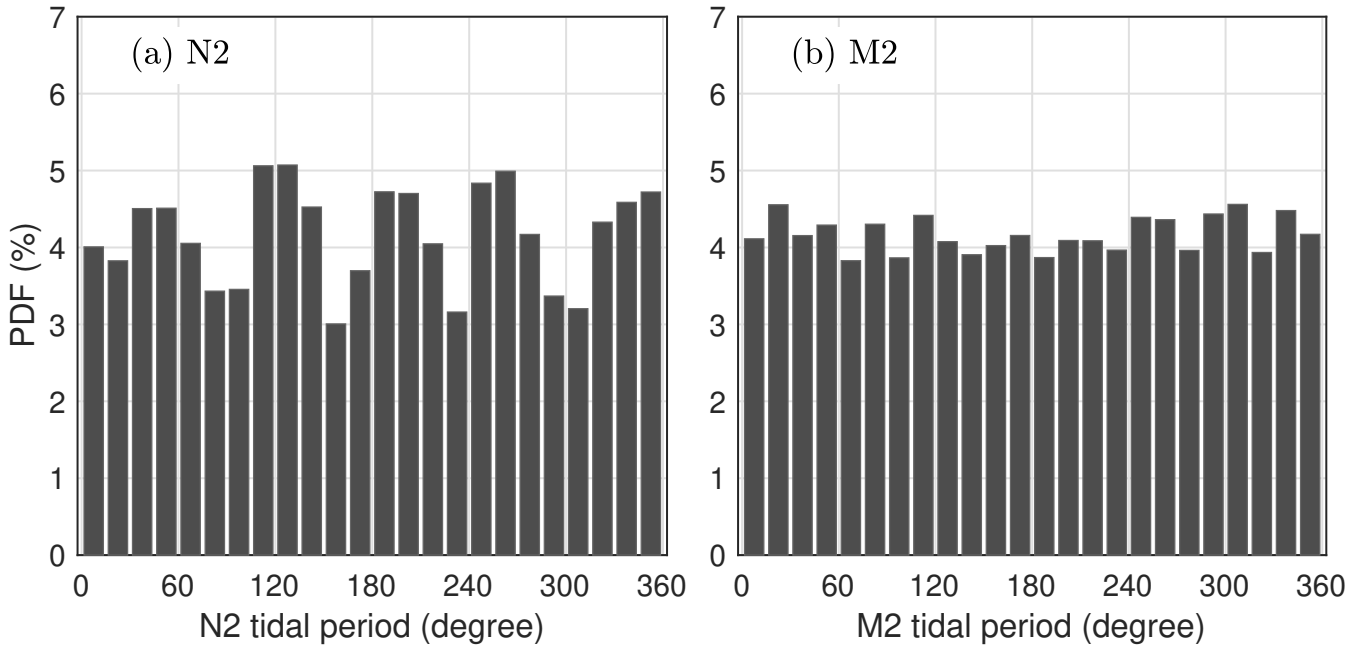
3

Figure 2. Histograms of the phase lags of the satellite SSH data over one N_2 (a) and M_2 (b) tidal period. This example is for one 160 km by 160 km window centered at 15°N, 160°W. There are about 7.84×10^4 SSH measurements in this window. From their observation times, the phase lags with respect to N_2 and M_2 are calculated.

Figure 2b shows the histogram with respect to the M_2 tidal cycle (12.4206 hours). The results show that the SSH data overall evenly distribute over one N_2 or M_2 tidal cycle, without extreme biases. In particular, their distribution on M_2 is smooth, suggesting that there is no tidal aliasing issues for M_2. Their distribution over N_2 is a little bumpy, suggesting that the resulting N_2 internal tides may have larger errors. The uneven distribution stems from the orbital configurations of the satellite missions. Fortunately, as shown in this study, the new mode-1 N_2 internal tides can overcome background noise.

2.2 Plane wave analysis

The core technique of our mapping procedure is plane wave analysis. By this method, internal tides are determined by fitting horizontal plane waves in one given fitting window (160 km by 160 km in this study), in contrast to harmonic analysis at one single site. This method has been described in detail in our previous studies (Zhao and Alford, 2009; Zhao, 2014; Zhao et al., 2016). For each tidal constituent, there may be multiple internal tides of arbitrary propagation directions at each site, due to their multiple source regions and long-range propagation. Plane wave analysis can resolve these internal tides by propagation direction. We will fit 5 mode-1 N_2 internal tidal waves at each site. Our 5-wave representor follows

$$\Sigma_{m=1}^{5} A_m \cos(k\, x \cos\theta_m + k\, y \sin\theta_m - \omega\, t - \phi_m), \tag{1}$$

4

where x and y are the east and north Cartesian coordinates, t is time, ω and k are the frequency and horizontal wavenumber of the target internal tides, respectively. Three parameters need to be determined for each internal tidal wave: amplitude A, phase ϕ, and direction θ. To determine one wave, the amplitude and phase of a single plane wave are determined by the least-squares fit in each compass direction (with $1°$ increment). When the resulting amplitudes are plotted as a function of direction in polar coordinates, an internal tidal wave appears to be a lobe. The direction of the first wave is thus determined from the biggest lobe. Thus, the amplitude A, phase ϕ, and propagation direction θ of one internal tidal wave are determined. Afterward, its signal is predicted and subtracted from the original data, which removes the wave itself and its side lobes. This procedure can be repeated to extract an arbitrary number of waves one by one. The resulting internal tidal waves are sorted with descending amplitudes.

The frequency (ω) and horizontal wavenumber (k) of the target internal tides are needed in plane wave analysis. The M_2 and N_2 tidal periods (equivalent to frequencies) are from the Moon's orbital motion around the Earth (Doodson, 1921; Pawlowicz et al., 2002). They are 12.4206 and 12.6583 hours, respectively. The local phase speed (equivalent to wavenumber) of the target internal tides is theoretically determined from the World Ocean Atlas 2018 (WOA18) (Boyer et al., 2018). The WOA18 provides climatological hydrographic profiles on a spatial grid of $0.25°$ latitude by $0.25°$ longitude. Ocean depth is based on the 1-arc-minute topography database constructed using in situ and satellite measurements (Smith and Sandwell, 1997). For given ocean depth and stratification profile, the vertical structures and eigenvalue speeds of internal tides are obtained by solving the Sturm-Liouville equation (Gill, 1982; Chelton et al., 1998)

$$\frac{d^2\Phi(z)}{dz^2} + \frac{N^2(z)}{c^2}\Phi(z) = 0, \tag{2}$$

subject to free-surface and rigid-bottom boundary conditions, where $N(z)$ is buoyancy frequency profile, and c is the eigenvalue speed. The phase speed c_p can be calculated from the eigenvalue speed following

$$c_p = \frac{\omega}{\sqrt{\omega^2 - f^2}}c, \tag{3}$$

where ω and f are the tidal and inertial frequencies, respectively. Note that the phase speed is a function of longitude and latitude (Zhao et al., 2016).

2.3 Mapping procedure

Our three-step mapping procedure consists of two rounds of plane wave analysis and a spatial two-dimensional (2D) bandpass filter in between (Zhao, 2020, 2021, 2022a, b). In this paper, the mapping process is illustrated by showing intermediate results in Figure 3. An interested reader is referred to the above papers for more details.

In step 1, mode-1 N_2 internal tides are mapped by plane wave analysis as described above. The N_2 internal tides are mapped from along-track SSH data onto a spatially regular grid. In this paper, our fitting window is chosen to be 160 km by 160 km, consistent with wavelengths of mode-1 N_2 internal tides. The resulting N_2 internal tides are at a $0.2°$ longitude by $0.2°$ latitude grid. At each grid point, five mode-1 N_2 internal tidal waves of arbitrary propagation directions are determined. The vector sum of these five waves gives the internal tide solution. Figure 3a shows the mode-1 N_2 internal tide field obtained. It gives

obvious internal tide signals (e.g., around the Hawaiian Ridge), but the nontidal noise is high. In step 2, the spatially regular N_2 internal tide field is cleaned by a 2D bandpass filter in overlapping 850 km by 850 km windows. The N_2 internal tide field is first converted to the 2D wavenumber spectrum by Fourier transform. The spectrum is truncated to [0.8 1.25] times the local wavenumber. The truncated spectrum is converted back to the internal tide field by inverse Fourier transform. Figure 3b shows the cleaned N_2 internal tide field. Now the N_2 internal tide signals are much cleaner. However, Figure 3b cannot resolve multiple internal tidal waves yet. In step 3, plane wave analysis is called again to decompose the filtered internal tide field into five internal waves of arbitrary propagation directions. The second-round plane wave analysis is same as the first-round plane wave analysis, except that the input is the filtered internal tide field in step 2. In the end, the resulting five waves are saved with their respective amplitudes, phases and directions. Figure 3c shows the 5-wave superimposed internal tide field. It is very similar to Figure 3b, because this step only decompose the internal tide field. The 5-wave decomposition allows us to separate internal tides of different propagation directions. They will be used to extract long-range internal tidal beams in the ocean (Section 3).

2.4 N_2 and M_2 internal tides

We map both the mode-1 N_2 and M_2 internal tides following the same 3-step procedure. They are constructed from the same satellite altimetry data, but using their respective wave parameters (frequency and wavenumber). Figure 4 shows the resulting N_2 and M_2 internal tide fields. Internal tides in shallow waters (<1000 m) are discarded. The new M_2 internal tides are almost identical to those obtained in previous studies using slightly different satellite data (Zhao, 2022b). Here we find that the N_2 and M_2 internal tides have similar spatial patterns, and that the N_2 amplitudes are about 20% of the M_2 amplitudes. The largest N_2 amplitudes are about 5 mm, compared to 20–30 mm for M_2 internal tides. To account for this factor, their colormap ranges are different by a factor of 5. Figure 4 gives SWOT ground tracks in its one-day fast-repeating phase (green lines). It shows that strong mode-1 N_2 internal tides occur under some SWOT swaths, for example, those off the California coast, in the New Caledonia region, in the western North Pacific, and on the Amazon continental shelf. In these regions, the N_2 internal tides cannot be neglected in the study of sub-mesoscale dynamics. Conversely, the upcoming SWOT data also offer a great opportunity to explore internal tides.

We have examined the possible cross-talk between the N_2 and M_2 internal tides in our mapping procedure. We map N_2 internal tides using two different data sets. The first is the original satellite altimetry SSH data set (Section 2.1). The second is the M_2-corrected data set. In other words, the M_2 internal tides are predicted using our empirical model and subtracted from the original data. We find that the resulting N_2 internal tides from the two data sets are almost the same. The variance of their differences is <1% that of the N_2 internal tides. Likewise, we map M_2 internal tides using both the original and N_2-corrected data sets, respectively, and find that the impact of N_2 on M_2 is negligible. Our analysis reveals that the N_2 and M_2 internal tides do not crosstalk in our mapping method. It is because the 27-year-long satellite data from 1993 to 2019 are sufficient long to unambiguously separate the N_2 and M_2 tidal constituents.
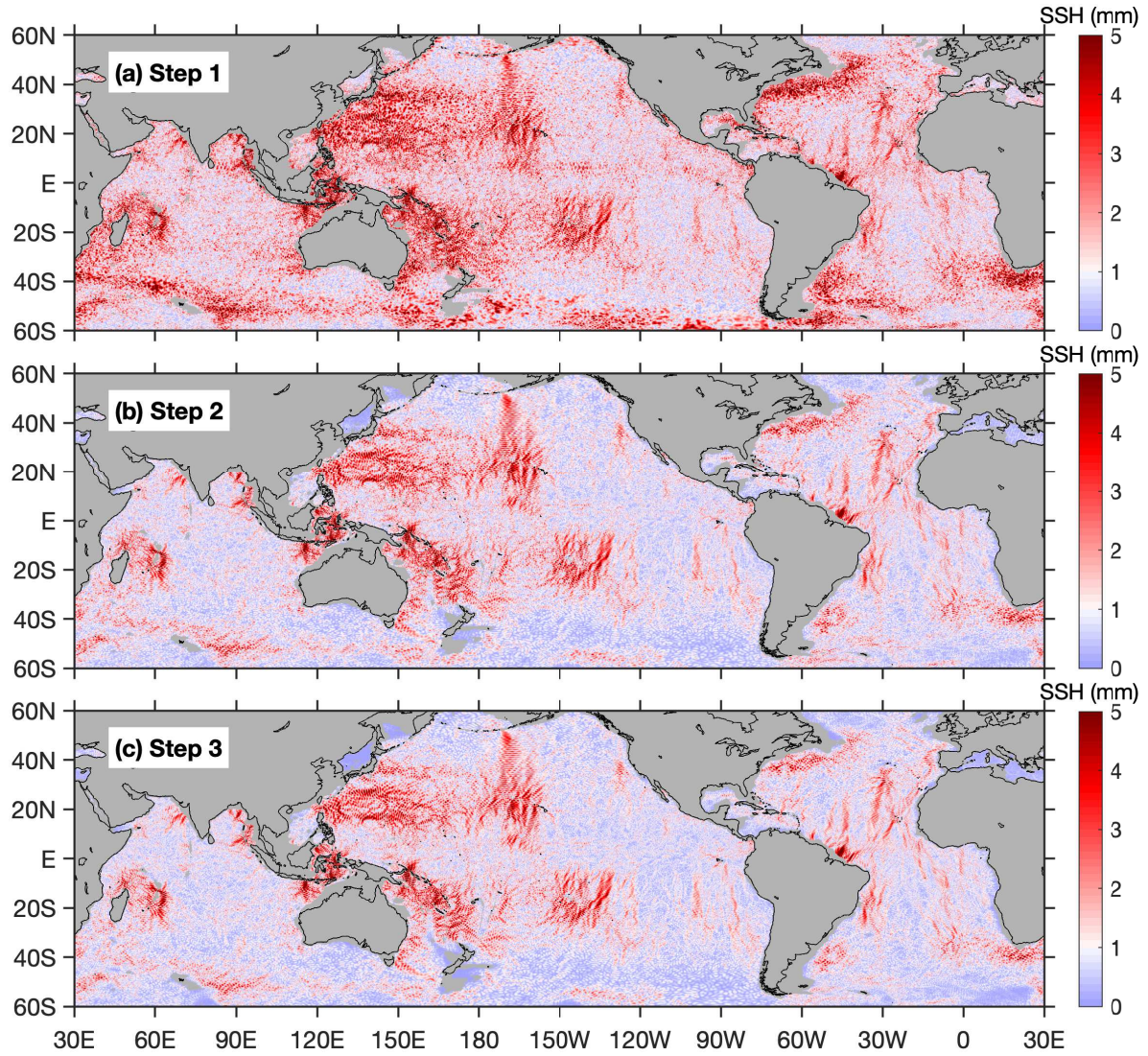
Figure 3. The 3-step mapping procedure. (a) Mode-1 N_2 internal tides are obtained by the first-round plane wave analysis. (b) Mode-1 N_2 internal tides are cleaned by 2D bandpass filtering. (c) Mode-1 N_2 internal tides are decomposed by the second-round plane wave analysis. Shown here is the 5-wave superposed amplitude.
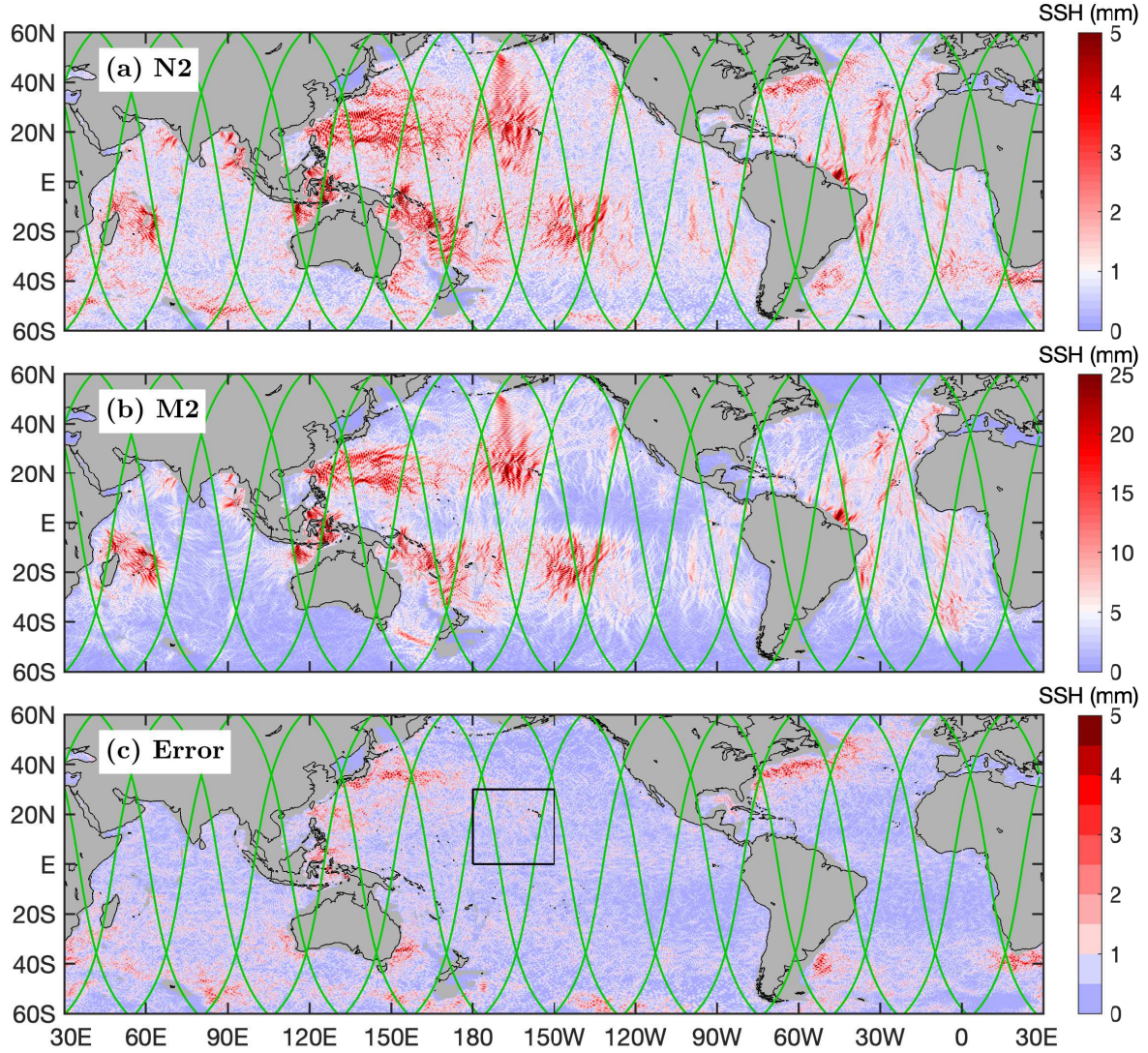
Figure 4. Internal tides and model errors. Shown are their SSH amplitudes. (a) N_2. (b) M_2. N_2 and M_2 have similar spatial patterns. The N_2 amplitudes are about 20% of the M_2 amplitudes. (c) Errors. The model errors are obtained by mapping internal tides with a tidal period of 12.6074 hours (Figure 5) using the same satellite altimetry data and the same mapping procedure. Green lines denote SWOT ground tracks in the fast-repeating phase. The mean SSH amplitude in the black box is given in Figure 5

2.5 Model errors

Model errors in our N_2 and M_2 internal tide models are estimated using background internal tides. In contrast that N_2 and M_2
internal tides are mapped using tidal periods of 12.6583 and 12.4206 hours, respectively, background internal tides are mapped
using the same satellite altimetry data, but for tidal periods between N_2 and M_2. Specifically, we map 13 sets of background
internal tides using 13 different tidal periods that are linearly interpolated between N_2 and M_2 (Figure 5). The other mapping
parameter, wavenumber (equivalently phase speed), can be obtained using Equation (3). The same strategy has been employed
to estimate barotropic tide errors. For example, Ray and Susanto (2016) study the spring-neap tidal cycles (MS_f and M_f) of
tidal mixing using satellite sea surface temperature data. Zaron et al. (2023) study the fortnightly variability of Chl-a using
satellite sea surface color data. In both studies, tidal errors are estimated using signals at fake or false tidal frequencies near the
real tidal constituents.

We thus obtain 13 background internal tides in the central Pacific (Figure 4c, box). Their regional mean SSH amplitudes
in this region are 0.8±0.1 mm, compared to 1.66 and 7.75 mm for N_2 and M_2 (Figure 5). Note that the SSH amplitudes of
the 13 background internal tides are almost same, showing no significant tidal cusps around the N_2 or M_2 internal tides. In
addition, we have calculated the correlation coefficients among these 15 sets of internal tides (including N_2 and M_2). All the
correlation coefficients are <0.05, suggesting that these background internal tides are independent with each other and with the
N_2 and M_2 internal tides. In other words, background internal tides are signals we obtain where there are no tidal constituents.
We suggest that the model errors in N_2 and M_2 can be represented by background internal tides. In this study, we pick one
tidal period (12.6074 hours) for a global run to obtain background internal tides (model errors), considering that a global run
is time consuming. Figure 4c gives the resulting background internal tides (model errors). It reveals that model errors are large
in regions of strong eddy kinetic energy (EKE), because model errors are mainly caused by EKE. Figure 4 shows that the N_2
internal tides are noisier than M_2, because the small-amplitude N_2 internal tides are easily affected by model errors. On global
average, the error variance is about 25% of the N_2 variance, and only 1% of the M_2 variance.

2.6 Model evaluation

Our N_2 and M_2 internal tide models are evaluated using independent satellite SSH data collected in 2020 and 2021. For
each SSH measurement of known time and location, the internal tide signal is predicted using the model under evaluation,
and subtracted from the SSH measurement. Variance reduction is the variance difference before and after the internal tide
correction. The variance reductions for all SSH measurements are binned into 2° by 2° boxes. The global map of N_2 variance
reduction is shown in Figure 6a. The M_2 internal tide model is evaluated in the same way and shown in Figures 6b. Note that
the colormap ranges for N_2 and M_2 differ by a factor of 25, that is, the square of the factor of their amplitudes.

In the evaluation, the true N_2 internal tides (variance σ_{N2}) in the model will remove the N_2 internal tides in the independent
data, leading to positive variance reduction. While the model errors (variance σ_ϵ) will increase the variance of the independent
data, leading to negative variance reduction. Together, we obtain positive variance reduction where $\sigma_{N2} > \sigma_\epsilon$, and negative
variance reduction where $\sigma_{N2} < \sigma_\epsilon$. Figure 6a shows that the global ocean is dominated by positive variance reduction, sug-
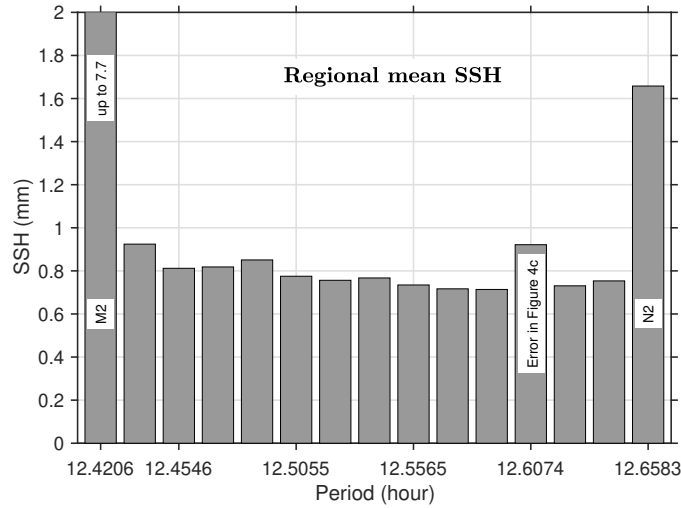
Figure 5. Histogram of regional mean SSH amplitudes. In the central Pacific Ocean ($0°$–$30°$N, $180°$–$150°$W), 15 sets of internal tides are determined using the same satellite data and following the same procedure. They are mapped using their respective periods and wavenumbers. Tidal periods of the 13 sets of background internal tides are linearly interpolated between N_2 and M_2.

gesting that the true N_2 internal tides are usually greater than model errors. In particular, in regions of strong N_2 internal tides such as the Hawaiian Ridge and the Amazon continental shelf, patches of positive variance reduction are observed, because the strong N_2 internal tides can overcome model errors. While negative variance reduction usually occurs in regions of weak N_2 internal tides such as the eastern equatorial Pacific and the Southern Ocean. The regions of strong EKE are dominated by

190   negative variance reduction, where weak N_2 internal tides are overwhelmed by large model errors (Figure 4c). For comparison, Figure 6b shows that the M_2 internal tide model causes positive variance reduction throughout the global ocean, except for regions of strong EKE or strong temporal variation (Zhao, 2021). It is because the strong M_2 internal tides are dominantly greater than the model errors $\sigma_{M2} > \sigma_\epsilon$. In summary, our N_2 internal tide model can reduce variance in most ocean regions, although the N_2 SSH amplitudes are just a few mm.

195   We further examine the relation between the N_2 variance reduction shown in Figure 6a and the variance difference between the N_2 model and the model error. Note that the model variance σ contains both N_2 internal tides and errors $\sigma = \sigma_{N2} + \sigma_\epsilon$, where the error variance σ_ϵ can be computed from the error map (Figure 4c). For the condition of greater N_2 variance $\sigma_{N2} > \sigma_\epsilon$, we should have $\sigma > 2\sigma_\epsilon$. We thus calculate the variance difference $\sigma - 2\sigma_\epsilon$ and show the global map in Figure 6c. To prove this relation, we examine the variance difference $\sigma - m \cdot \sigma_\epsilon$ for m ranging from 0.5 to 3.5 with a step of 0.1. For each variance

200   difference map, we calculate its correlation coefficient with the N_2 variance reduction (Figure 6a). We get the best spatial correlation when the factor m is 2, consistent with our theoretical analysis above. Note that all the above analyses are based on the $2°$ by $2°$ binned values. Figure 6d shows the mask region where the model variance is greater than twice the error variance, indicating regions where the N_2 model can be used to make internal tide correction. It covers regions of strong N_2 and M_2
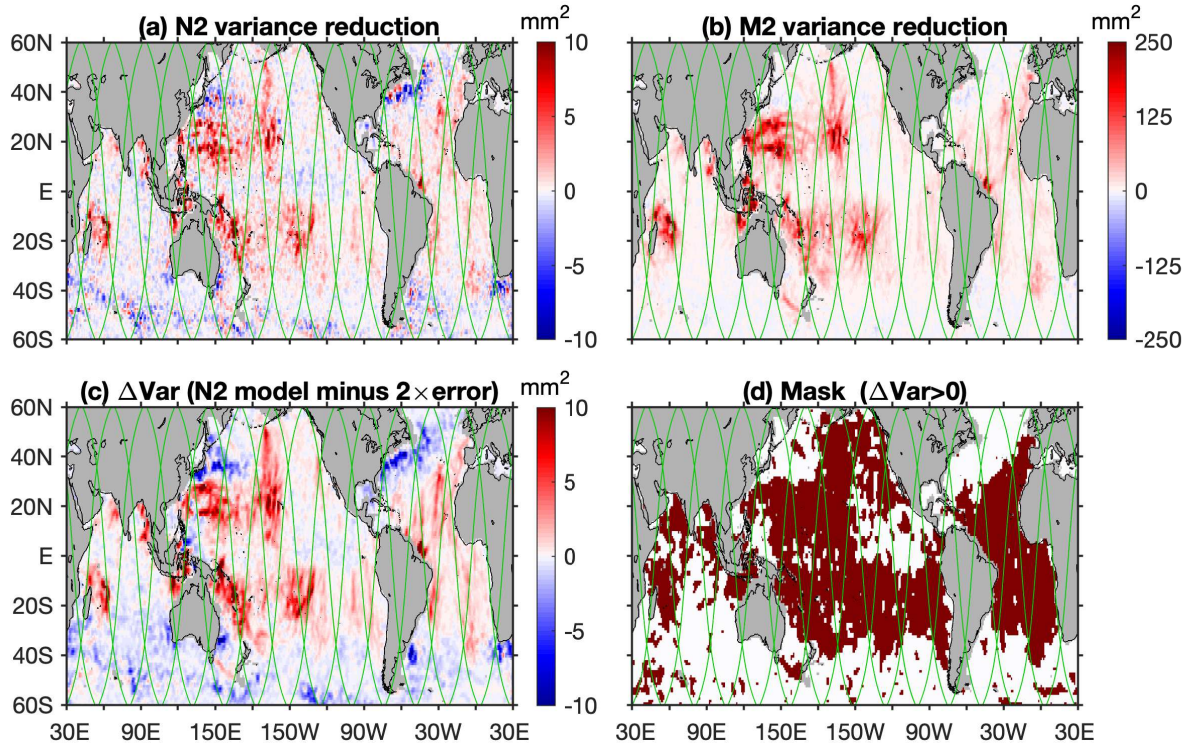
Figure 6. Model evaluation. Internal tide models are evaluated using independent altimetry data in 2020 and 2021. Shown are variance reductions binned in $2°$ by $2°$ boxes. (a) N_2. (b) M_2. (c) Difference between the N_2 model variance and twice the error variance. The factor is chosen to obtain the best spatial correlation between (a) and (c). (d) Mask where the model variance is greater than twice the error variance, indicating the region where the N_2 model can be used to make internal tide correction. Green lines denote SWOT ground tracks in the fast-repeating phase.

internal tides such as the Hawaiian Ridge, off the California coast, the Amazon continental shelf, the western North Pacific, and the New Caledonia.

We next examine the performance of the N_2 and M_2 internal tide models in making internal tide correction for SWOT. In Figure 6, the green lines denote the SWOT ground tracks in its daily fast-repeating phase. We interpolate the N_2 and M_2 variance reductions onto the SWOT ground tracks (neglecting its swath), and integrate along-track variance reductions. For N_2, the integrated variance reductions in and outside the mask region are 500 and -160 mm^2, respectively. The negative variance reduction outside the mask region suggests that the N_2 model does not work well there. Fortunately, the N_2 model can make internal tide correction for SWOT in the mask region where the N_2 internal tides can overcome model errors. For M_2, the along-track integrations in and outside the mask region are 1.9×10^4 and 0.1×10^4 mm^2, respectively. The numbers suggest that the M_2 model performs well both in and outside the mask region, because the M_2 internal tides dominate errors throughout the global ocean.
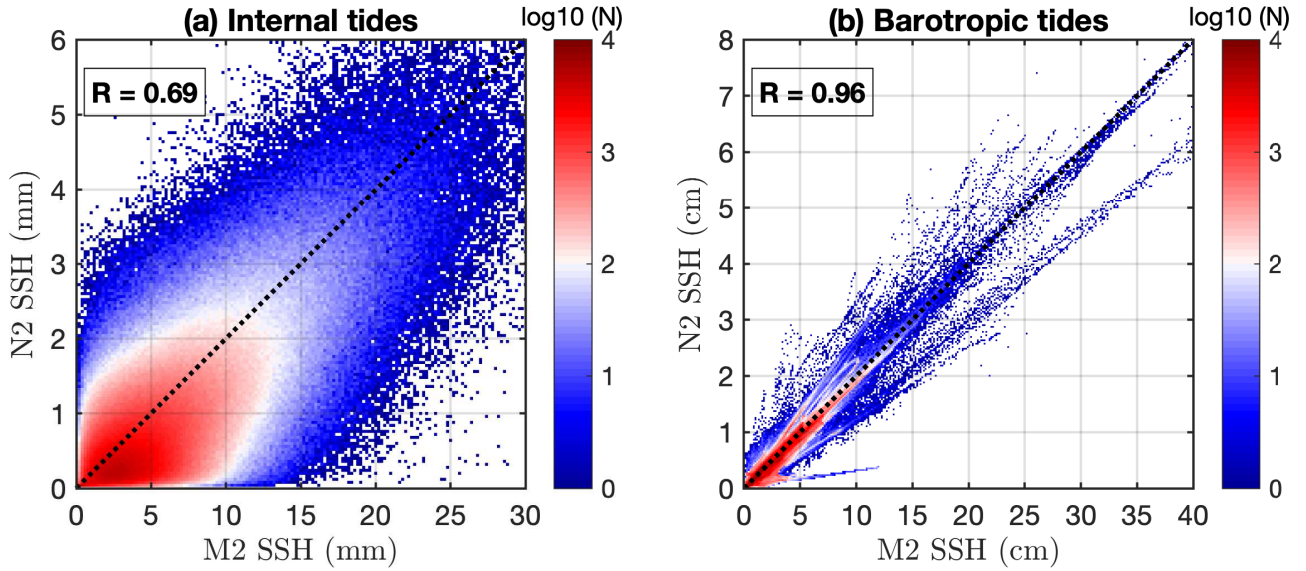
11

Figure 7. Comparisons of N_2 and M_2 amplitudes. (a) Internal tides. (b) Barotropic tides. Shown is data density in logarithmic scale. Their correlation coefficients (R) are calculated. For both the barotropic and internal tides, the N_2 amplitudes are about 20% of the M_2 amplitudes.

3   Results

3.1   Global distribution

Our mode-1 N_2 model reveals that N_2 internal tides are widespread in the global ocean (Figure 4a). In the Indian Ocean, they are observed in the Arabian Sea, the Bay of Bengal, and the Madagascar-Mascarene region. In the Pacific Ocean, N_2 internal tides occur in regions such as the French Polynesian Ridge, the Hawaiian Ridge, the Indonesian seas, the western South Pacific, and the western North Pacific. In the Atlantic Ocean, N_2 internal tides appear in regions including the Azores region, the Amazon shelf, the Bay of Biscay, and the Vitoria-Trindade Ridge. Our M_2 model reveals that mode-1 M_2 internal tides are observed in the same regions (Figure 4b). The N_2 and M_2 internal tides have similar spatial patterns, but the N_2 amplitudes are about 20% of the M_2 amplitudes. To further quantify their relation, we give in Figure 7a the scatter plot of the N_2 and M_2 SSH amplitudes. It shows that the N_2 and M_2 amplitudes largely follow the diagonal line with a ratio of 5. Their correlation coefficient is 0.69 (R in Matlab function *corrcoef*).

We extract the N_2 and M_2 barotropic tides from TPXO.8 (Egbert and Erofeeva, 2002) and show them in Figure 8. We find that the N_2 and M_2 barotropic tides have similar spatial patterns, and that the N_2 amplitudes are about 20% of the M_2 amplitudes. We examine the relation between the N_2 and M_2 barotropic tides as well. Figure 7b shows the scatter plot of the N_2 and M_2 barotropic amplitudes. It shows that N_2 and M_2 have a very tight relation, with their correlation coefficient being 0.96. Egbert and Ray (2003) show that the M_2 and N_2 barotropic-to-baroclinic energy conversion maps have similar spatial patterns, and that their amplitudes differ by a factor of 25 (see their Figure 1). The N_2 and M_2 relation (spatial pattern and
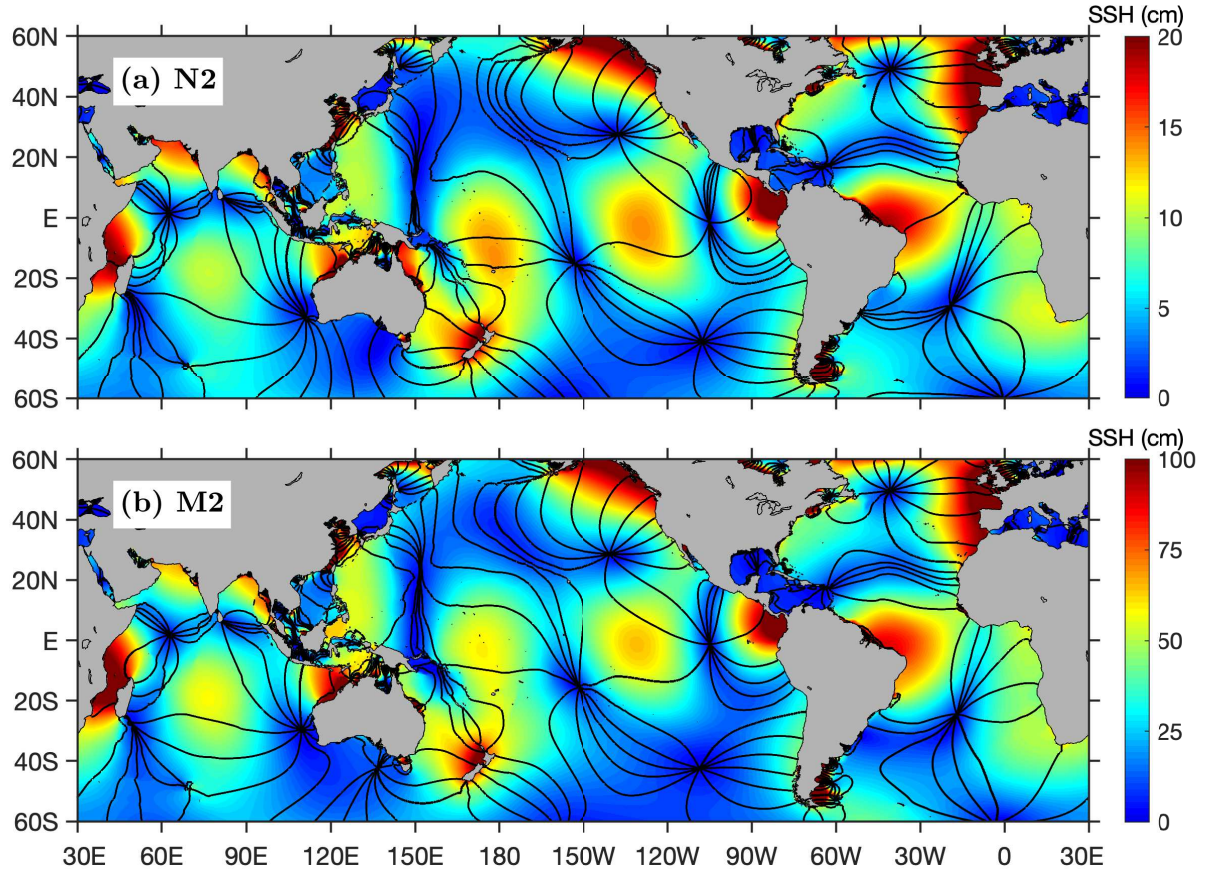
Figure 8. N_2 and M_2 barotropic tides from TPXO.8 (Egbert and Erofeeva, 2002). Colors show amplitude. Black lines show co-phase charts at $30°$ intervals. N_2 and M_2 have similar spatial patterns, and the N_2 amplitudes are about 20% of the M_2 amplitudes.

amplitude ratio) is the same for both barotropic and baroclinic tides. Because N_2 and M_2 have close tidal periods (12.6583 and 12.4206 hours), their generations over the same topographic features should be the same. In addition, it is reasonable that the N_2 and M_2 internal tides have a relatively weak relation (Figure 7a), because the long-range propagation of internal tides is
235   affected by an inhomogeneous ocean environment.

3.2 Long-range beams

In this section, we study the long-range mode-1 N_2 internal tidal beams. We have fitted five mode-1 N_2 internal tidal waves at each grid point by plane wave analysis. Taking advantage of the 5-wave fits, we can decompose the N_2 internal tide field into the northward ($0°$–$180°$ anti-clockwise from due east) and southward ($180°$–$360°$) components by propagation direction. Each
240   component contains internal tidal waves with propagation directions falling in the given range (Figure 9). The decomposed components clearly show well-defined long-range N_2 internal tidal beams, which are characterized by larger amplitudes and
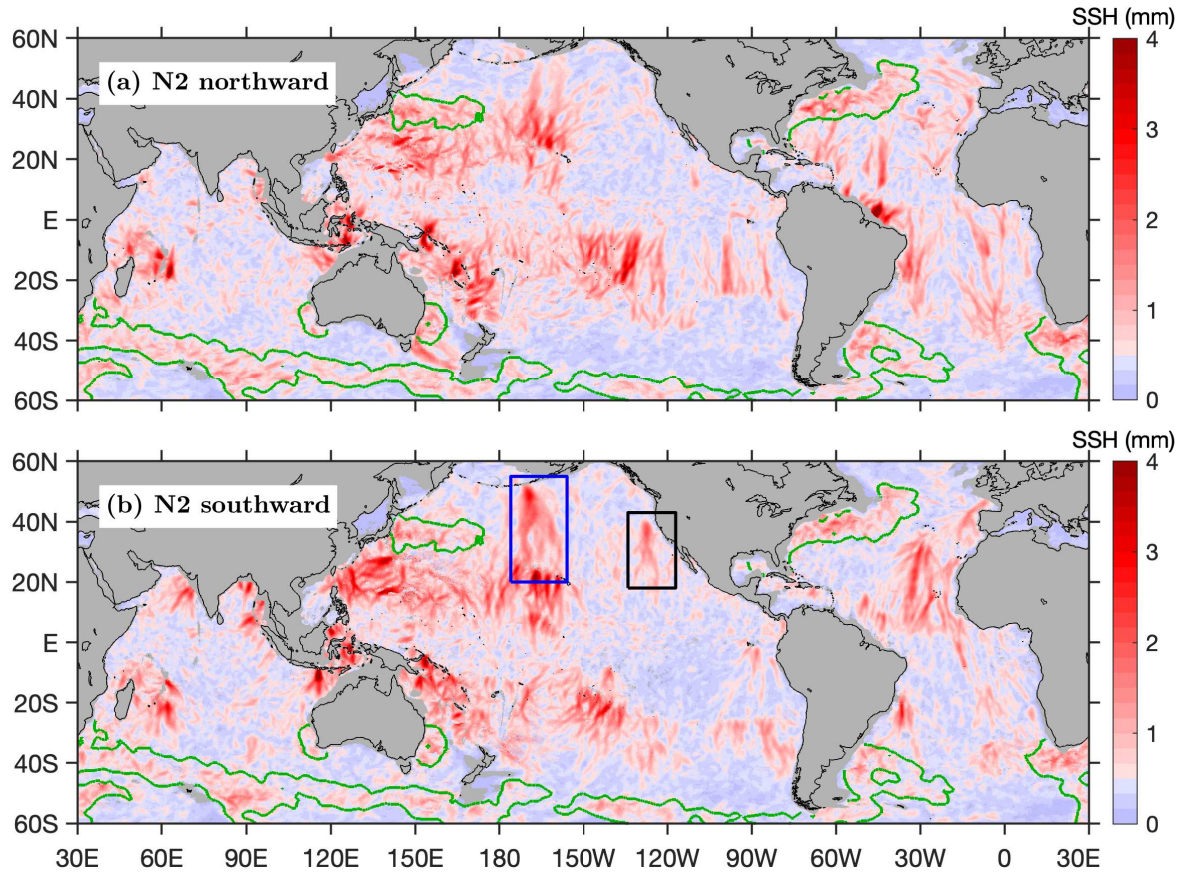
13

Figure 9. Decomposed N_2 internal tide fields. (a) Northward component (directional range: $0°$–$180°$ anti-clockwise from due east). (b) Southward component (directional range: $180°$–$360°$). Internal tides in shallow waters (<1000 m) are discarded. Green contours indicate regions of strong boundary currents, where the N_2 internal tides have larger errors.

cross-beam co-phase lines (not shown here for clarity; see Figures 10 and 11). There are numerous long-range N_2 internal tidal beams, which radiate from the strong generation sites mentioned above. For example, northward N_2 beams are observed to originate from the French Polynesian Ridge, the Macquarie Ridge, the Amazon shelf, and so on. Southward N_2 beams are observed to originate from the Andaman Islands, the Lombok Strait, the Hawaiian Ridge, the French Polynesian Ridge, the Mendocino Ridge, the Azores Islands, among others. Note that the M_2 long-range internal tidal beams have been well studied in previous studies (Zhao et al., 2016, Figure 5 therein). To avoid repetition, the M_2 internal tidal beams are not shown here. Together, we observe that the N_2 and M_2 internal tides have similar long-range beams. In this study, we examine two long-range internal tidal beams as examples.

First, we examine the southward internal tides from the Amukta Pass, Alaska. The M_2 long-range beam from Amukta Pass has been studied recently (Zhao, 2022b). Figure 10a shows the southward N_2 internal tides in the central North Pacific (Figure
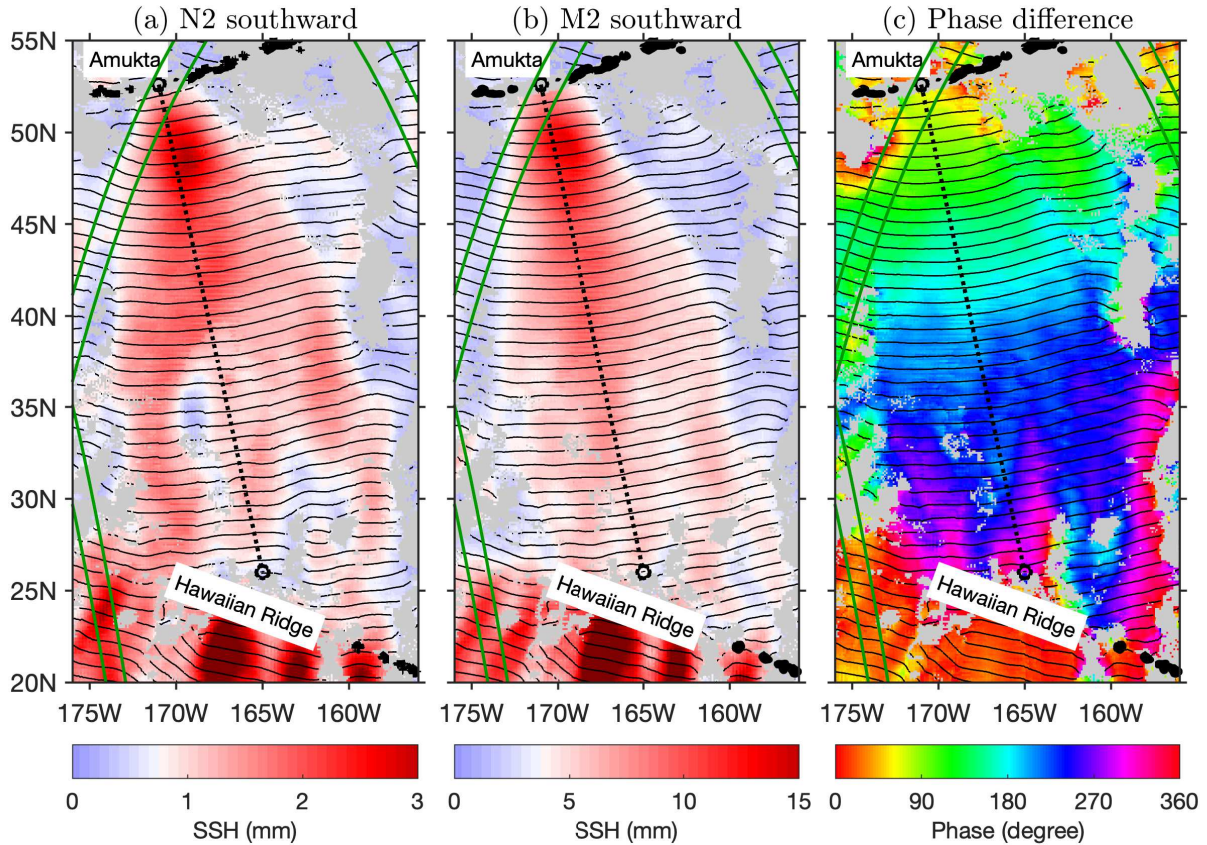
Figure 10. Southward (180°–360°) internal tides from Amukta Pass, Alaska. (a) N_2 internal tides. (b) M_2 internal tides. Black contours show the 0° and 180° co-phase lines. Intervals between two neighboring co-phase lines are half wavelengths. (c) Phase difference between N_2 and M_2. Black contours show the M_2 co-phase lines as in (b). Weak internal tides are discarded (M_2 <1 mm; N_2 <0.2 mm). Both N_2 and M_2 internal tides can propagate over 3000 km from the Aleutian Ridge to the Hawaiian Ridge. Along the 3000-km-long path (dashed lines), their phase difference increases from 65° to 305°. Green lines denote the 120-km-wide SWOT swaths in the fast-repeating phase.

9b, blue box). For comparison, the southward M_2 internal tides are shown in Figure 10b. Both tidal constituents can travel from the Aleutian island chain to the Hawaiian Ridge over 3,000 km away. Their propagation directions are about $-78°$ from due east. The black lines shows the 0° and 180° co-phase charts. Figure 10c shows their phase difference, which increases with 255 propagation, because N_2 internal tides travel faster than M_2 internal tides according to Equation (3). In the propagation, their phase difference increases with propagation. Along the dashed line from source (52.6°N, 189°E) to far field (26°N, 195°E), their phase difference increases from 65° to 305°. The overall phase change is 240°. It takes about 18 tidal cycles for the N_2 and M_2 internal tides to travel along the path.

Figure 11 shows southward internals tides in the region off the California Coast (Figure 9b, black box). This region is chosen 260 for a detailed investigation, because it contains one site for the SWOT calibration/validation field experiment. The green lines
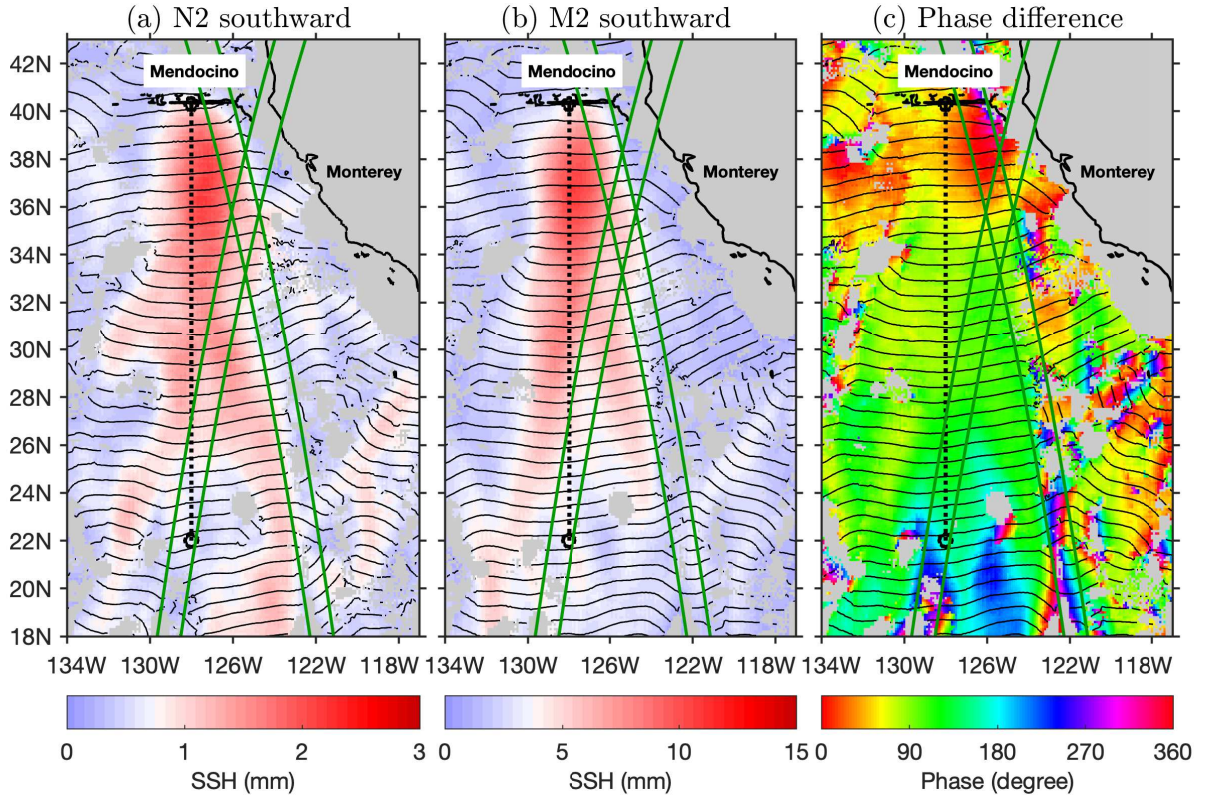
15

Figure 11. Southward ($180°$–$360°$) internal tides off the U.S. West Coast. (a) N_2 internal tides. (b) M_2 internal tides. Colors show SSH amplitudes. Black contours indicate the $0°$ and $180°$ co-phase lines. Southward internal tides are mainly from the Mendocino Ridge. Weak internal tides are discarded ($M_2 < 1$ mm; $N_2 < 0.2$ mm). Internal tides in shallow waters (< 1000 m) are discarded. (c) Phase difference between N_2 and M_2. Green lines denote two 120-km-wide SWOT swaths in the fast-repeating phase.

in this figure indicate the SWOT swaths in its fast-repeating phase (Wang et al., 2022). The cross-over region of the ascending and descending swaths is the SWOT calibration/validation site. This region is dominated by the southward internal tides from the Mendocino Ridge. Note that this region is also affected by internal tides in other propagation directions (Zhao et al., 2019). Additionally, there are southwestward internal tides from the Monterey Bay. The two internal tidal beams intersect around the SWOT experiment site. As explained earlier, our N_2 model can make internal tide correction for SWOT. Figure 11 shows that N_2 and M_2 internal tides are very similar, although the N_2 fluxes are much weaker. Both N_2 and M_2 beams can be tracked from $40°$N to $20°$N for > 2000 km. They both bifurcate around $32°$N near Fieberling Seamounts ($32.5°$N, $232.3°$E) for unknown reasons. The dashed line delineates the beam from $40.3°$N to $22°$N along $128°$W. This line is about 2000 km long. Along this line, the N_2 and M_2 phase difference increases from $40°$ to $160°$ over about 14 M_2 or N_2 tidal cycles.

3.3 Energy and energy flux

We calculate the depth-integrated energy flux of mode-1 N_2 internal tide from their SSH amplitudes and a transfer function (F_n). The transfer function is calculated using the WOA18 climatological hydrography and the Sturm-Liouville equation (Zhao and Alford, 2009; Zhao et al., 2016). The same calculation method has also been derived by Geoffroy and Nycander (2022). In this study, we repeat our method (previously for mode-1 M_2 internal tides) to obtain the transfer function for mode-1 N_2 internal tides. It is a function of ocean depth, tidal frequency, mode number, latitude, and stratification. The transfer functions for N_2 and M_2 are very close, because their tidal periods are close. At each grid point, we thus obtain five energy fluxes for the five internal tidal waves following $F = \frac{1}{2}F_n A^2$, where A is the SSH amplitude. The vector sum of the five energy fluxes gives the final energy flux at this site. In this study, we compare the N_2 and M_2 internal tide energy fluxes in two regions. An interested reader can examine other ocean regions. We show that their energy fluxes have similar spatial patterns. The results show that the mode-1 N_2 internal tides can be observed by satellite altimetry, although their are much weaker than the M_2 internal tides. Following the same procedure, we have computed the depth-integrated internal tide energies from SSH amplitudes. The globally integrated area-weighted energies for the N_2 and M_2 internal tides are 1.8 and 30.9 PJ, respectively. The N_2-to-M_2 ratio is about 5.8%, larger than the theoretical value of 4%, because N_2 contains larger error variance. As explained earlier, the error variance is about 25% of the N_2 variance, but only 1% of the M_2 variance.

Figure 12 shows the N_2 and M_2 energy fluxes in the western South Pacific. In this study, it is trimmed to 30°S–0°, 145°E–135°W. Colors show flux magnitudes, and black arrows show flux vectors. This region is chosen because (1) it features various topographic obstacles such as mid-ocean ridge and island chain, and (2) the New Caledonia region is one site for SWOT calibration/validation (Bendinger et al., 2023). There are numerous N_2 and M_2 internal tidal beams in this region. They are dominantly generated over topographic features. For example, N_2 and M_2 internal tidal beams radiate from many straits in the Coral Sea (Tchilibou et al., 2020). The internal tidal beams can be in any horizontal propagation direction. From the French Polynesian Ridge, internal tides mainly propagate southward and northward. From the Kermadec Arc and the New Caledonia, the outgoing internal tidal beam usually travel eastward or westward. The energy fluxes of N_2 and M_2 internal tides have similar spatial patterns. Figure 12 shows seven SWOT swaths in this region (green lines). Among them, the two swaths in the New Caledonia region (black box) overlap with strong N_2 internal tides. In addition, the two swaths lie cross the French Polynesian Ridge, where one should pay an attention to N_2 and M_2 internal tides in the study of mesoscale and sub-mesoscale processes.

Figure 13 shows the N_2 and M_2 energy fluxes in the North Atlantic Ocean (2°S–53°N, 58°W–3°W). Figure 13 is in the same format as Figure 12. Internal tides in this region have attracted much attention in recent years (Vic et al., 2018; Köhler et al., 2019; Löb et al., 2020). In particular, internal tides on the Amazon continental shelf have been intensively studied recently, partly because of the co-existence of internal tides and internal solitary waves (Egbert and Erofeeva, 2021; Tchilibou et al., 2022; Assene et al., 2023). Our satellite observation reveals that strong N_2 and M_2 internal tides occur around notable topographic features including the Mid-Atlantic Ridge, the Amazon continental shelf, the Azores region, the Bay of Biscay, Canary Islands, and the Cape Verde islands. The longest internal tidal beams for both N_2 and M_2 are the southward internal
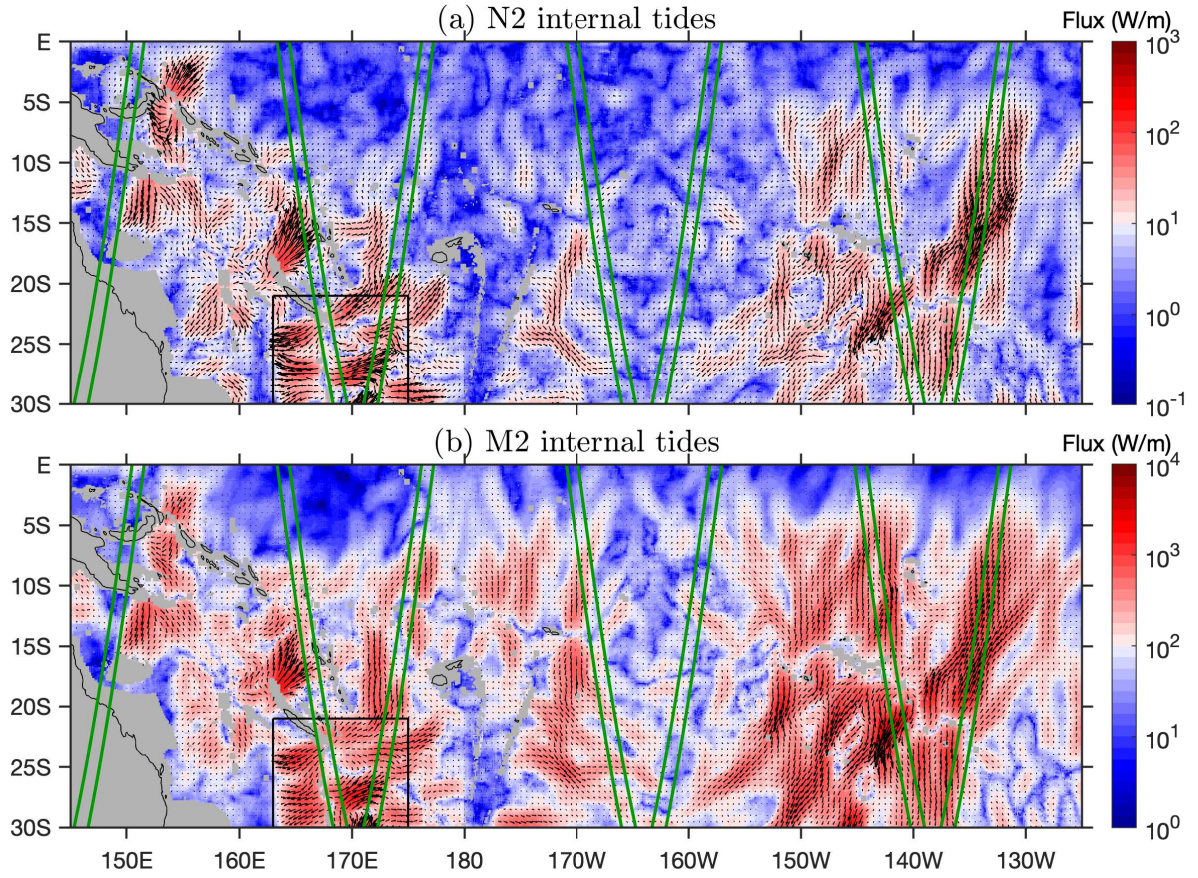
Figure 12. Internal tide energy fluxes in the western South Pacific. (a) N_2 internal tides. (b) M_2 internal tides. Colors show flux magnitudes and black arrows show flux vectors. Internal tides in shallow waters (<1000 m) are discarded (gray shading). Green lines indicate SWOT swaths in the fast-repeating phase.

tidal beams from the Azores (Zhao, 2016; Köhler et al., 2019). The two beams can be tracked over 2000 km. In this region,
305   there are four SWOT swaths in its fast-repeating phase, which overlap remarkable N_2 and M_2 internal tidal beams.

4   Summary

In this study, we constructed empirical models for mode-1 N_2 and M_2 internal tides from satellite altimetry. Among them, N_2 is the larger lunar elliptical semidiurnal constituent and the fifth largest oceanic tidal constituent. It is induced by the Moon's elliptical orbit. Its amplitudes are about 20% of the M_2 amplitudes. The mode-1 N_2 internal tides have sub-centimeter-scale
310   SSH amplitudes. We can extract weak N_2 internal tides, because we use a larger altimetry data set and a newly-developed mapping procedure. First, we use the multiyear multisatellite altimetry data from 1993 to 2019. The combined data are about 100 satellite-years long, which can significantly suppress nontidal errors. Second, we extract mode-1 N_2 internal tides by a
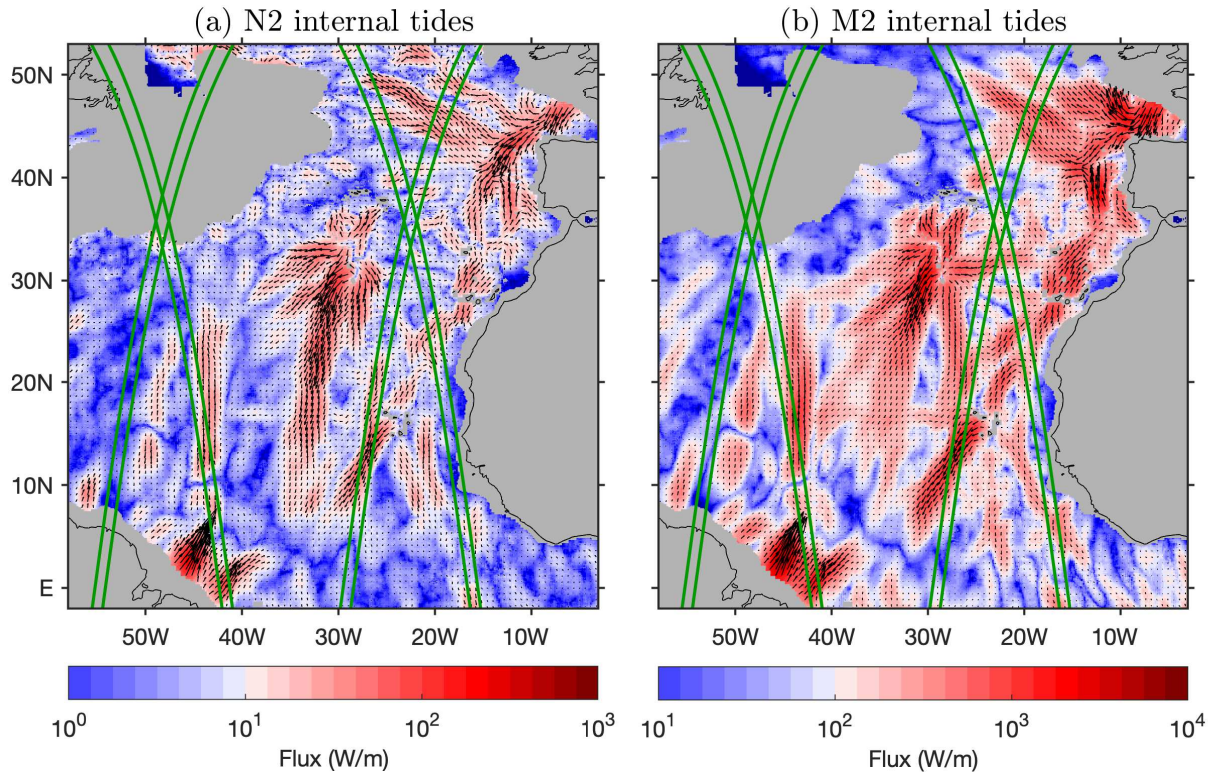
Figure 13. As in Figure 12 but for internal tide energy flux in the North Atlantic Ocean.

three-step mapping procedure, which cleans internal tides using known frequency and wavenumber of the target internal tide. In consequence, satellite altimetry can observe mode-1 N_2 internal tides with mm-scale SSH amplitudes. Our N_2 internal tide model is still noisy. Future improvements can be made with more and more satellite altimetry data becoming available.

We estimated errors in the N_2 and M_2 internal tide models using background internal tides. Specifically, background internal tides are mapped using the same altimetry data but for tidal periods between N_2 and M_2. In this study, we construct a global map of model errors using a tidal period of 12.6074 hours (N_2 minus 3 minute). The model errors are usually <1 mm in the global ocean, with the global mean error being about 0.7 mm. Large errors usually occur in regions of strong EKE, since the model errors mainly come from the leaked EKE. On global average, the error variance is about 25% of the N_2 model variance, but only 1% of the M_2 model variance.

Our satellite observation revealed some basic features of the global N_2 internal tides. We found that the N_2 and M_2 internal tides have similar spatial patterns, and that the N_2 amplitudes are about 20% of the M_2 amplitudes. Both features are determined by their barotropic counterparts. We found that both N_2 and M_2 internal tides can propagate hundreds to thousands of kilometers in the open ocean, but at different phase speeds. We examined regional N_2 internal tides and revealed rich informa-

tion on their generation and propagation. We suggest that including N_2 internal tides can better simulate the temporal variation of internal tide energetics with the lunar elliptical orbital motion.

Our N_2 and M_2 internal tide models have been evaluated using independent altimetry data in 2020 and 2021. The M_2 model can cause variance reduction throughout the global ocean, because the M_2 internal tides dominate the model errors. In contrast, the N_2 model can cause variance reduction in regions of strong N_2 internal tides where they can overcome errors. We found that the N_2 model performs well in the mask region where the N_2 model variance is greater than twice the error variance. We showed that the N_2 and M_2 models work well along the SWOT fast-repeating tracks. We propose to make internal tide correction for SWOT in the mask region.

Last but not least, we demonstrated in this study that our mapping technique can construct a reliable mode-1 N_2 internal tide model using 100 satellite-years altimetry data. We have applied our mapping technique to the first baroclinic mode of other minor tidal constituents and higher baroclinic mode of other major tidal constituents, and obtained clear internal tide signals. We have tried mapping mode-2 N_2 internal tides around the Hawaiian Ridge (185–205°E, 18–28°N). However, the resulting model is noisy, as expected. In this region, the mean amplitude of mode-1 N_2 internal tides is about 2.5 mm. The mean mode-2 N_2 amplitude would be around 1 mm, using a ratio of 2.5 from mode-1 and -2 M_2 internal tides. The $\sim$1-mm mode-2 N_2 signal cannot overcome the $\sim$0.7-mm noise. It is expected that the low-noise SWOT data along 120-km-wide swaths will greatly improve the observation of minor tidal constituents and higher baroclinic modes.

Author contributions. This paper is completed by the sole author.

Competing interests. The author has declared there are no competing interests.

References

Arbic, B. K.: Incorporating tides and internal gravity waves within global ocean general circulation models: A review, Progress in Oceanography, 206, 102 824, https://doi.org/10.1016/j.pocean.2022.102824, 2022.

Assene, F., Koch-Larrouy, A., Dadou, I., Tchilibou, M., Morvan, G., Chanut, J., Vantrepotte, V., Allain, D., and Tran, T.-K.: Internal tides off the Amazon shelf Part I : importance for the structuring of ocean temperature during two contrasted seasons, EGUsphere, 2023, 1–46, https://doi.org/10.5194/egusphere-2023-418, 2023.

Bendinger, A., Cravatte, S., Gourdeau, L., Brodeau, L., Albert, A., Tchilibou, M., Lyard, F., and Vic, C.: Regional modeling of internal tide dynamics around New Caledonia: energetics and sea surface height signature, EGUsphere, 2023, 1–53, https://doi.org/10.5194/egusphere-2023-361, 2023.

Boyer, T. P., García, H. E., Locarnini, R. A., Zweng, M. M., Mishonov, A. V., Reagan, J. R., Weathers, K. A., Baranova, O. K., Paver, C. R., Seidov, D., and Smolyar, I. V.: World Ocean Atlas 2018, Tech. rep., NOAA National Centers for Environmental Information, https://www.ncei.noaa.gov/archive/accession/NCEI-WOA18, 2018.

Byun, D.-S. and Hart, D. E.: A monthly tidal envelope classification for semidiurnal regimes in terms of the relative proportions of the S_2, N_2, and M_2 constituents, Ocean Science, 16, 965–977, https://doi.org/10.5194/os-16-965-2020, 2020.

Chelton, D. B., deSzoeke, R. A., Schlax, M. G., El Naggar, K., and Siwertz, N.: Geographical variability of the first baroclinic Rossby radius of deformation, Journal of Physical Oceanography, 28, 433–460, https://doi.org/10.1175/1520-0485(1998)028<0433:GVOTFB>2.0.CO;2, 1998.

de Lavergne, C., Vic, C., Madec, G., Roquet, F., Waterhouse, A. F., Whalen, C. B., Cuypers, Y., Bouruet-Aubertot, P., Ferron, B., and Hibiya, T.: A Parameterization of Local and Remote Tidal Mixing, Journal of Advances in Modeling Earth Systems, 12, e2020MS002 065, https://doi.org/10.1029/2020MS002065, 2020.

Doodson, A. T.: The harmonic development of the tide-generating potential, Proceedings of the Royal Society A, 100, 305–329, https://doi.org/10.1098/rspa.1921.0088, 1921.

Dushaw, B. D.: An empirical model for mode-1 internal tides derived from satellite altimetry: Computing accurate tidal predictions at arbitrary points over the world oceans, Tech. rep., Applied Physics Laboratory, University of Washington, 2015.

Dushaw, B. D., Howe, B. M., Cornuelle, B. D., Worcester, P. F., and Luther, D. S.: Barotropic and Baroclinic Tides in the Central North Pacific Ocean Determined from Long-Range Reciprocal Acoustic Transmissions, Journal of Physical Oceanography, 25, 631–647, 1995.

Egbert, G. D. and Erofeeva, S. Y.: Efficient inverse modeling of barotropic ocean tides, Journal of Atmospheric and Oceanic Technology, 19, 183–204, 2002.

Egbert, G. D. and Erofeeva, S. Y.: An Approach to Empirical Mapping of Incoherent Internal Tides With Altimetry Data, Geophysical Research Letters, 48, e2021GL095 863, https://doi.org/10.1029/2021GL095863, 2021.

Egbert, G. D. and Ray, R. D.: Significant dissipation of tidal energy in the deep ocean inferred from satellite altimeter data, Nature, 405, 775–778, https://doi.org/10.1038/35015531, 2000.

Egbert, G. D. and Ray, R. D.: Semi-diurnal and diurnal tidal dissipation from TOPEX/Poseidon altimetry, Geophysical Research Letters, 30, 1907, https://doi.org/10.1029/2003GL017676, 2003.

Fu, L.-L. and Ubelmann, C.: On the Transition from Profile Altimeter to Swath Altimeter for Observing Global Ocean Surface Topography, Journal of Atmospheric and Oceanic Technology, 31, 560–568, https://doi.org/10.1175/JTECH-D-13-00109.1, 2014.

Geoffroy, G. and Nycander, J.: Global Mapping of the Nonstationary Semidiurnal Internal Tide Using Argo Data, Journal of Geophysical Research: Oceans, 127, e2021JC018 283, https://doi.org/10.1029/2021JC018283, 2022.

Gill, A. E.: Atmosphere-Ocean Dynamics, Academic Press, 1982.

390   Jayne, S. R. and St. Laurent, L. C.: Parameterizing tidal dissipation over rough topography, Geophysical Research Letters, 28, 811–814, https://doi.org/10.1029/2000GL012044, 2001.

Kelly, S. M., Waterhouse, A. F., and Savage, A. C.: Global Dynamics of the Stationary M_2 Mode-1 Internal Tide, Geophysical Research Letters, 48, e2020GL091 692, https://doi.org/10.1029/2020GL091692, 2021.

Köhler, J., Walter, M., Mertens, C., Stiehler, J., Li, Z., Zhao, Z., von Storch, J.-S., and Rhein, M.: Energy Flux Observations in an Internal Tide

395   Beam in the Eastern North Atlantic, Journal of Geophysical Research: Oceans, 124, 5747–5764, https://doi.org/10.1029/2019JC015156, 2019.

Löb, J., Köhler, J., Mertens, C., Walter, M., Li, Z., von Storch, J.-S., Zhao, Z., and Rhein, M.: Observations of the Low-Mode Internal Tide and Its Interaction With Mesoscale Flow South of the Azores, Journal of Geophysical Research: Oceans, 125, e2019JC015 879, https://doi.org/10.1029/2019JC015879, 2020.

400   MacKinnon, J. A., Zhao, Z., Whalen, C. B., Waterhouse, A. F., Trossman, D. S., Sun, O. M., Laurent, L. C. S., Simmons, H. L., Polzin, K., Pinkel, R., Pickering, A., Norton, N. J., Nash, J. D., Musgrave, R., Merchant, L. M., Melet, A. V., Mater, B., Legg, S., Large, W. G., Kunze, E., Klymak, J. M., Jochum, M., Jayne, S. R., Hallberg, R. W., Griffies, S. M., Diggs, S., Danabasoglu, G., Chassignet, E. P., Buijsman, M. C., Bryan, F. O., Briegleb, B. P., Barna, A., Arbic, B. K., Ansong, J. K., and Alford, M. H.: Climate Process Team on Internal Wave-Driven Ocean Mixing, Bull. Amer. Meteor. Soc., 98, 2429–2454, https://doi.org/10.1175/BAMS-D-16-0030.1, 2017.

405   Melet, A., Legg, S., and Hallberg, R.: Climatic Impacts of Parameterized Local and Remote Tidal Mixing, J. Climate, 29, 3473–3500, https://doi.org/10.1175/JCLI-D-15-0153.1, 2016.

Morrow, R., Fu, L.-L., Ardhuin, F., Benkiran, M., Chapron, B., Cosme, E., d'Ovidio, F., Farrar, J. T., Gille, S. T., Lapeyre, G., Le Traon, P.-Y., Pascual, A., Ponte, A., Qiu, B., Rascle, N., Ubelmann, C., Wang, J., and Zaron, E. D.: Global Observations of Fine-Scale Ocean Surface Topography With the Surface Water and Ocean Topography (SWOT) Mission, Frontiers in Marine Science, 6,

410   https://doi.org/10.3389/fmars.2019.00232, 2019.

Munk, W. H. and Wunsch, C.: Abyssal recipes II: Energetics of tidal and wind mixing, Deep-Sea Res. I, 45, 1977–2010, https://doi.org/10.1016/S0967-0637(98)00070-3, 1998.

Pawlowicz, R., Beardsley, B., and Lentz, S.: Classical tidal harmonic analysis including error estimates in MATLAB using T_TIDE, Computers and Geosciences, 28, 929–937, 2002.

415   Pollmann, F., Nycander, J., Eden, C., and Olbers, D.: Resolving the horizontal direction of internal tide generation, Journal of Fluid Mechanics, 864, 381–407, https://doi.org/10.1017/jfm.2019.9, 2019.

Pujol, M.-I., Faugère, Y., Taburet, G., Dupuy, S., Pelloquin, C., Ablain, M., and Picot, N.: DUACS DT2014: the new multi-mission altimeter data set reprocessed over 20 years, Ocean Science, 12, 1067–1090, https://doi.org/10.5194/os-12-1067-2016, 2016.

Qiu, B., Chen, S., Klein, P., Wang, J., Torres, H., Fu, L.-L., and Menemenlis, D.: Seasonality in transition scale from balanced to unbalanced

420   motions in the world ocean, Journal of Physical Oceanography, 48, 591–605, https://doi.org/10.1175/JPO-D-17-0169.1, 2018.

Ray, R. D. and Byrne, D. A.: Bottom pressure tides along a line in the southeast Atlantic Ocean and comparisons with satellite altimetry, Ocean Dynamics, 60, 1167–1176, https://doi.org/10.1007/s10236-010-0316-0, 2010.

Ray, R. D. and Susanto, R. D.: Tidal mixing signatures in the Indonesian Seas from high-resolution sea surface temperature data, Geophysical Research Letters, 43, 8115–8123, https://doi.org/10.1002/2016GL069485, 2016.

Ray, R. D. and Zaron, E.: M$_2$ internal tides and their observed wavenumber spectra from satellite altimetry, Journal of Physical Oceanography, 46, 3–22, https://doi.org/10.1175/JPO-D-15-0065.1, 2016.

Smith, W. H. F. and Sandwell, D. T.: Global sea floor topography from satellite altimetry and ship depth soundings, Science, 277, 1956–1962, https://doi.org/10.1126/science.277.5334.1956, 1997.

Taburet, G., Sanchez-Roman, A., Ballarotta, M., Pujol, M.-I., Legeais, J.-F., Fournier, F., Faugere, Y., and Dibarboure, G.: DUACS DT2018: 25 years of reprocessed sea level altimetry products, Ocean Science, 15, 1207–1224, https://doi.org/10.5194/os-15-1207-2019, 2019.

Tchilibou, M., Gourdeau, L., Lyard, F., Morrow, R., Koch Larrouy, A., Allain, D., and Djath, B.: Internal tides in the Solomon Sea in contrasted ENSO conditions, Ocean Science, 16, 615–635, https://doi.org/10.5194/os-16-615-2020, 2020.

Tchilibou, M., Koch-Larrouy, A., Barbot, S., Lyard, F., Morel, Y., Jouanno, J., and Morrow, R.: Internal tides off the Amazon shelf during two contrasted seasons: interactions with background circulation and SSH imprints, Ocean Science, 18, 1591–1618, https://doi.org/10.5194/os-18-1591-2022, 2022.

Ubelmann, C., Carrere, L., Durand, C., Dibarboure, G., Faugère, Y., Ballarotta, M., Briol, F., and Lyard, F.: Simultaneous estimation of ocean mesoscale and coherent internal tide sea surface height signatures from the global altimetry record, Ocean Science, 18, 469–481, https://doi.org/10.5194/os-18-469-2022, 2022.

Vic, C., Naveira Garabato, A. C., Green, J. A. M., Spingys, C., Forryan, A., Zhao, Z., and Sharples, J.: The lifecycle of semidiurnal internal tides over the northern Mid-Atlantic Ridge, Journal of Physical Oceanography, 48, 61–80, https://doi.org/10.1175/JPO-D-17-0121.1, 2018.

Vic, C., Naveira Garabato, A. C., Green, J. A. M., Waterhouse, A. F., Zhao, Z., Melet, A., de Lavergne, C., Buijsman, M. C., and Stephenson, G. R.: Deep-ocean mixing driven by small-scale internal tides, Nature Communications, 10, 2099, https://doi.org/10.1038/s41467-019-10149-5, 2019.

Wang, J., Fu, L.-L., Qiu, B., Menemenlis, D., Farrar, J. T., Chao, Y., Thompson, A. F., and Flexas, M. M.: An Observing System Simulation Experiment for the Calibration and Validation of the Surface Water Ocean Topography Sea Surface Height Measurement Using In Situ Platforms, Journal of Atmospheric and Oceanic Technology, 35, 281–297, https://doi.org/10.1175/JTECH-D-17-0076.1, 2018.

Wang, J., Fu, L.-L., Haines, B., Lankhorst, M., Lucas, A. J., Farrar, J. T., Send, U., Meinig, C., Schofield, O., Ray, R., Archer, M., Aragon, D., Bigorre, S., Chao, Y., Kerfoot, J., Pinkel, R., Sandwell, D., and Stalin, S.: On the Development of SWOT In Situ Calibration/Validation for Short-Wavelength Ocean Topography, Journal of Atmospheric and Oceanic Technology, 39, 595–617, https://doi.org/10.1175/JTECH-D-21-0039.1, 2022.

Whalen, C. B., de Lavergne, C., Naveira Garabato, A. C., Klymak, J. M., MacKinnon, J. A., and Sheen, K. L.: Internal wave-driven mixing: governing processes and consequences for climate, Nature Reviews Earth & Environment, https://doi.org/10.1038/s43017-020-0097-z, 2020.

Wood, F. J.: The Strategic Role of Perigean Spring Tides: In Nautical History and North American Coastal Flooding, 1635-1976, Department of Commerce, National Oceanic and Atmospheric Administration, National Ocean Survey, 1978.

Wunsch, C.: Internal tides in the ocean, Rev. Geophys. Space Phys., 13, 167–182, 1975.

Zaron, E. D.: Baroclinic tidal sea level from exact-repeating mission altimetry, Journal of Physical Oceanography, 49, 193–210, https://doi.org/10.1175/JPO-D-18-0127.1, 2019.

Zaron, E. D., Capuano, T. A., and Koch-Larrouy, A.: Fortnightly variability of Chl a in the Indonesian Seas, Ocean Science, 19, 43–55, https://doi.org/10.5194/os-19-43-2023, 2023.

Zhao, Z.: Internal tide radiation from the Luzon Strait, Journal of Geophysical Research: Oceans, 119, 5434–5448, https://doi.org/10.1024/2014JC010014, 2014.

Zhao, Z.: Internal tide oceanic tomography, Geophysical Research Letters, 43, 9157–9164, https://doi.org/10.1002/2016GL070567, 2016.

Zhao, Z.: Southward internal tides in the northeastern South China Sea, Journal of Geophysical Research: Oceans, 125, e2020JC01 654, https://doi.org/10.1029/2020JC016554, 2020.

Zhao, Z.: Seasonal mode-1 M_2 internal tides from satellite altimetry, Journal of Physical Oceanography, 51, 3015–3035, https://doi.org/10.1175/JPO-D-21-0001.1, 2021.

Zhao, Z.: Satellite estimates of mode-1 M_2 internal tides uisng nonrepeat altimetry missions, Journal of Physical Oceanography, 52, 3065–3076, https://doi.org/10.1175/JPO-D-21-0287.1, 2022a.

Zhao, Z.: Development of the Yearly Mode-1 M_2 Internal Tide Model in 2019, Journal of Atmospheric and Oceanic Technology, 39, 463 – 478, https://doi.org/10.1175/JTECH-D-21-0116.1, 2022b.

Zhao, Z. and Alford, M. H.: New altimetric estimates of mode-1 M_2 internal tides in the central North Pacific Ocean, Journal of Physical Oceanography, 39, 1669–1684, https://doi.org/10.1175/2009JPO3922.1, 2009.

Zhao, Z., Alford, M. H., Girton, J. B., Rainville, L., and Simmons, H. L.: Global observations of open-ocean mode-1 M_2 internal tides, Journal of Physical Oceanography, 46, 1657–1684, https://doi.org/10.1175/JPO-D-15-0105.1, 2016.

Zhao, Z., Wang, J., Menemenlis, D., Fu, L.-L., Chen, S., and Qiu, B.: Decomposition of the multimodal multidirectional M_2 internal tide field, Journal of Atmospheric and Oceanic Technology, 36, 1157–1173, https://doi.org/10.1175/JTECH-D-19-0022.1, 2019.